Journal of Cluster Science (2018) 29:951–958
https://doi.org/10.1007/s10876-018-1404-4

ORIGINAL PAPER

Cyan-Blue Luminescence and Antiferromagnetic Coupling of CN-Bridged Tetranuclear Complex Based on Manganese(III) Schiff Base and Hexacyanoferrate(III)

Adem Donmez[1,2] · Mustafa Burak Coban[3,4] · Hulya Kara[1,3]

Received: 18 April 2018 / Published online: 1 June 2018

Abstract

A new tetranuclear cyanide-bridged Mn^{III}–Fe^{III} complex based on manganese(III) Schiff base and hexacyanoferrate(III) units, $[Mn(L)(MeOH)_2][\{Mn(L)\}\{Fe(CN)_6\}\{Mn(L)(MeOH)\}].2MeOH$, [$H_2L$ = *N*,*N*′-bis(2-hydroxy-1-naphthalidenato)-1,2-diaminopropane] (**1**), has been synthesized and characterized by elemental analysis, UV–Vis, FT-IR, PXRD, single crystal X-ray analyses, magnetic and photoluminescence measurements. Complex **1** consist of one trinuclear cyanido-bridged anion, in which $[Fe(CN)_6]^{3-}$ anion bridge $[Mn(L)]^+$ and $Mn(L)(MeOH)\}]^+$ cations via two C≡N groups in the *cis* positions, and also one isolated manganese $[Mn(L)(MeOH)_2]^+$ cation. DC magnetic susceptibility and magnetization studies showed that complex **1** indicates an antiferromagnetic coupling between low-spin Fe(III) and high-spin Mn(III) through the cyanide bridges. In addition, the complex **1** displays a strong cyan-blue luminescence emission in the solid state condition at room temperature. This behavior might be seen easily from the chromaticity diagram. Thus, the complex may be a good promising cyan-blue OLED developing electroluminescent materials for flatted or curved panel display applications due to the fact that it has such features.

Keywords Magnetism · Photoluminescence · X-ray analyses · Cyano-bridged · Mn^{III}–Fe^{III} compound

Introduction

Since the beginning of the twenty-first century, research on the multidimensional polymetallic functional materials that shows luminescence and magnetic properties have been a major focus of interest among scientists [1–5]. The main reason for this interest is due to the existence of their potential applications and devices as molecular switches, high-density memory materials, luminescence materials, non-linear optics and so on [6]. Among all these coordination polymers, one of the most important types of magnetic system commonly used in their application areas, cyanide-bridged Mn^{III}–Fe^{III} complexes have also received much attention because their molecular topological structures and the nature of the magnetic coupling between neighbouring metal ions through the cyanide bridge can be controlled and predicted relatively readily [7–10]. In the meantime, the transition metal complexes which especially shows the luminescence properties have been widely explored for developing in many technological applications areas such as organic light emitting devices, as probes in fluorescence lifetime imaging microscopy and sensors [11].

Electronic supplementary material The online version of this article (https://doi.org/10.1007/s10876-018-1404-4) contains supplementary material, which is available to authorized users.

✉ Hulya Kara
hkara@balikesir.edu.tr

[1] Department of Physics, Molecular Nano-Materials Laboratory, Mugla Sitki Kocman University, 48050 Mugla, Turkey

[2] Scientific Research Projects Coordination Unit, Mugla Sitki Kocman University, 48050 Mugla, Turkey

[3] Department of Physics, Balikesir University, 10145 Balikesir, Turkey

[4] Center of Sci and Tech App and Research, Balikesir University, 10145 Balikesir, Turkey

Schiff base molecular sensors used for the exact detection of the transition metal ions are great importance for the applications of fundamental science fields such as molecular chemistry and biology [12].

In recent years, the construction and synthesis of Mn^{III}–Fe^{III} complexes in nanoscale ranges have gained great importance and have been done an extensive research for the aim of fully clarify their magnetic, and structural properties and providing interesting molecular magnetic samples such as single-molecule magnets and single chain magnets, electric signal detectable samples such as sensors and luminescent probes, conductive or capable of energy conversion samples such as organic light emitting diode [13, 14]. In this context, our research group and others have studied the synthesis, crystal structure and magnetic properties of cyanide-bridged Mn^{III}–Fe^{III} complexes based on $[Fe(CN)_6]^{3-}$ and $[Mn^{III}(SB)]^{+}$ [15–19]. But, according to Cambridge Structural Database (CSD version 5.39, Nov 2017 updates), there is only one report which is published by our research group on their photoluminescence properties [20]. In view of the importance luminescence properties of these complexes, the synthesis of a new tetranuclear cyanide-bridged Mn^{III}–Fe^{III} complex along with single crystal X-ray structure, solid-state UV, IR, photoluminescence and magnetic study is presented here.

Experimental

Caution Perchlorate salts are potentially explosive and should only be handled in small quantities.

Materials and Measurements

All chemicals were purchased from Sigma-Aldrich. Elemental (C, H, N) analyses were carried out by standard methods with a LECO, CHNS-932 analyzers. FTIR spectra were measured with a Perkin-Elmer Spectrum 65 instrument in the range of 4000–600 cm^{-1}. Solid-state UV–Vis spectra were measured with an Ocean Optics Maya 2000-PRO spectrometer. Solid state photoluminescence spectra were measured at room temperature with an ANDOR SR500i-BL Photoluminescence Spectrometer, equipped with a triple grating and an air-cooled CCD camera as a detector. The measurements were done using the excitation source (349 nm) of a Spectra physics Nd:YLF laser with a 5 ns pulse width and 1.3 mJ of energy per pulse as the source. DC magnetic measurements were measured between 2 and 300 K at a field of 1.0 T using a Quantum Design model MPMS computer-controlled SQUID magnetometer. The data were corrected for sample holder contribution and diamagnetism of the sample using Pascal constants. The effective magnetic moments were calculated by the equation $\mu_{eff} = 2.828\ (\chi_m T)^{1/2}$ [21] where χ_m, the molar magnetic susceptibility, was set equal to M_m/H [21]. Powder X-ray measurements were performed using Cu-K_α radiation ($\lambda = 1.5418$ Å) on a Bruker-AXS D8-Advance diffractometer equipped with a secondary monochromator. The data were collected in the range $5° < 2\theta < 50°$ in θ–θ mode with a step time of ns ($5\ s < n < 10\ s$) and step width of 0.02°.

Synthesis of H_2L and Complex 1

The Schiff base ligand, H_2L, was synthesized by reaction of 1,2-diamino propane (1 mmol, 0.074 g) with 2-hydroxy-1-naphthaldehyde (2 mmol, 0.344 g) in ethanol (100 mL) according to the literature [22]. The monomeric Mn(III) complex was prepared by mixing manganese(III) acetate dihydrate, Schiff base ligand (H_2L) and $NaClO_4$ in ethanol/methanol/H_2O in a molar ratio of 1:1:1.5 according to the method reported previously [23]. Complex **1** has been prepared by mixing of the monomeric Mn(III) complex (0.1 mmol) in methanol (20 ml) with $K_3[Fe(CN)_6]$ (0.1 mmol) in H_2O (20 ml) at room temperature. The resulting solution was filtered and the filtrate was kept in the dark for a month. The resulting red block crystals were collected by filtration, washed with water and dried in the air. The synthetic route of the complex **1** is outlined in Scheme 1. Analysis calculated for H_2L $\{C_{25}H_{22}N_2O_2\}$ (yield 80%): C 78.51, H 5.80, N 7.32%. Found: C 78.52, H 5.83, N 7.34%. IR (cm^{-1}): ν(O–H) = 3064, ν(C = N) = 1614–1541, ν(C–H) = 2981–2937, ν(C–$O_{phenolic}$)- = 1494–1401. UV–Vis: λ_{max}/nm: 388. Analysis calculated for complex **1** $\{C_{86}H_{80}N_{12}O_{11}Mn_3Fe\}.\{3.(CH_3OH)\}$ (yield 65%): C 60.24, H 5.23, N 9.47%. Found: C 60.22, H 5.27, N 9.43%. IR (cm^{-1}): ν(C = N) = 1599–1540, ν(C≡N) = 2108, ν(C–H) = 3053–2928, ν(C–$O_{phenolic}$) = 1509–1408. UV–Vis: λ_{max}/nm: 310, 469.

X-ray Structure Determination

Diffraction measurement was made on a Bruker ApexII Kappa CCD diffractometer using graphite monochromated Mo-K_α radiation ($\lambda = 0.71073$ Å) at 293 K for **1**. The intensity data were integrated using the APEXII program [24]. Absorption correction was applied based on equivalent reflections using SADABS [25]. The structure was solved by direct methods using SHELXS [26] and refined by full–matrix least–squares based on $|F_{obs}|^2$ using SHELXL [27], in the Olex2 program [28]. All non-hydrogen atoms were assigned anisotropic displacement parameters. Hydrogen atoms were included in idealized positions with isotropic displacement parameters constrained to 1.5 times the U_{equiv} of their attached carbon atoms for methyl hydrogens, and 1.2 times the U_{equiv} of

Scheme 1 Schematic diagram of **1**

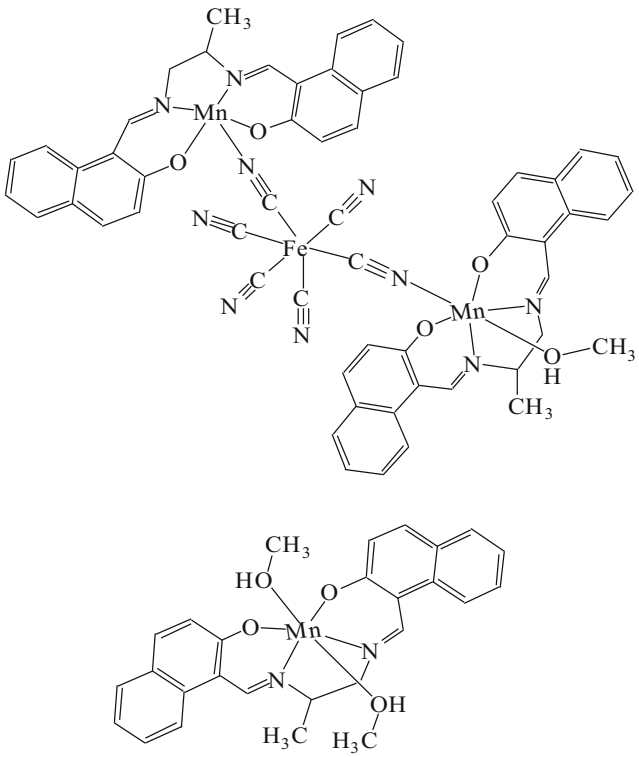

their attached carbon atoms for all others. The details of the supramolecular π-interactions and hydrogen bond geometry were investigated with a PLATON 1.17 program [29]. The crystal data and structure refinement details for **1** are listed in Table 1. The three methanol molecules in the crystal lattice appear to be disordered, and it was difficult to model reliably their positions and distribution. Therefore, the MASK function of the OLEX2 program was used to eliminate the contribution of the electron density in the solvent region from the intensity data, and the solvent-free model was employed for the final refinement. The three methanol molecules were not included in the total atomic formula in Table 1 and their atoms are not included in the list of atoms in Table 2. Crystallographic data for the

Table 1 Details of the data collection and refinement parameters for **1**

Empirical formula	$C_{86}H_{80}N_{12}O_{11}Mn_3Fe$
Formula weight	1678.29
Crystal system	Monoclinic
Space group	$P2_1/n$
a/Å	11.598(2)
b/Å	22.905(5)
c/Å	30.028(6)
α/°	90
β/°	100.57(3)
γ/°	90
Volume/Å^3	7841(3)
Z	4
ρ_{calc} g/cm^3	1.422
μ/mm^{-1}	0.723
Index ranges	$-15 \le h \le 15, -29 \le k \le 29, -38 \le l \le 38$
Reflections collected	87,926
Independent reflections	17,865
Goodness-of-fit on F^2	1.02
Final R indexes [I > = 2σ (I)]	$R_1 = 0.13$, $wR_2 = 0.32$

Table 2 Some selected bond lengths [Å] and angles [°] for **1**

Fe1–C76	1.919 (12)	Mn2–O4	1.860 (7)
Fe1–C77	1.943 (12)	Mn2–O5	2.352 (7)
Fe1–C78	1.947 (9)	Mn2–N3	1.976 (8)
Fe1–C79	1.927 (10)	Mn2–N4	1.960 (10)
Fe1–C83	1.924 (12)	Mn2–N10	2.235 (10)
Fe1–C84	1.928 (11)	Mn3–O6	1.863 (7)
Mn1–O1	1.875 (7)	Mn3–O7	1.887 (7)
Mn1–O2	1.873 (6)	Mn3–O8	2.260 (8)
Mn1–N1	1.963 (8)	Mn3–O9	2.234 (8)
Mn1–N2	1.952 (8)	Mn3–N11	1.974 (9)
Mn1–N5	2.143 (9)	Mn3–N12	1.948 (9)
Mn2–O3	1.881 (7)		
C76–Fe1–C77	178.2 (4)	O3–Mn2–N10	95.4 (4)
C76–Fe1–C78	88.7 (4)	O4–Mn2–O3	93.4 (3)
C76–Fe1–C79	93.3 (5)	O4–Mn2–O5	86.8 (3)
C76–Fe1–C83	88.7 (4)	O4–Mn2–N3	174.3 (4)
C76–Fe1–C84	93.2 (4)	O4–Mn2–N4	91.2 (4)
C77–Fe1–C78	89.8 (4)	O4–Mn2–N10	98.0 (3)
C79–Fe1–C77	88.2 (5)	N3–Mn2–O5	90.1 (3)
C79–Fe1–C78	177.9 (5)	N3–Mn2–N10	84.9 (3)
C79–Fe1–C84	87.2 (4)	N4–Mn2–O5	86.7 (4)
C83–Fe1–C77	90.2 (5)	N4–Mn2–N3	83.8 (4)
C83–Fe1–C78	90.6 (4)	N4–Mn2–N10	90.6 (4)
C83–Fe1–C79	90.2 (5)	N10–Mn2–O5	174.6 (3)
C83–Fe1–C84	176.9 (4)	O6–Mn3–O7	95.3 (3)
C84–Fe1–C77	87.9 (4)	O6–Mn3–O8	90.4 (3)
C84–Fe1–C78	91.9 (4)	O6–Mn3–O9	91.8 (3)
O1–Mn1–N1	89.4 (3)	O6–Mn3–N11	173.4 (3)
O1–Mn1–N2	163.0 (3)	O6–Mn3–N12	91.2 (3)
O1–Mn1–N5	102.9 (3)	O7–Mn3–O8	89.3 (3)
O2–Mn1–O1	92.9 (3)	O7–Mn3–O9	88.1 (3)
O2–Mn1–N1	163.8 (3)	O7–Mn3–N11	91.2 (3)
O2–Mn1–N2	90.6 (3)	O7–Mn3–N12	173.4 (3)
O2–Mn1–N5	97.5 (3)	O9–Mn3–O8	176.8 (3)
N1–Mn1–N5	97.7 (3)	N11–Mn3–O8	90.7 (3)
N2–Mn1–N1	82.7 (3)	N11–Mn3–O9	87.4 (3)
N2–Mn1–N5	93.1 (3)	N12–Mn3–O8	89.3 (3)
O3–Mn2–O5	86.8 (3)	N12–Mn3–O9	93.0 (3)
O3–Mn2–N3	91.2 (3)	N12–Mn3–N11	82.3 (4)
O3–Mn2–N4	171.9 (4)		

structural analyses have been deposited with the Cambridge Crystallographic Data Centre, CCDC No. 1836581. These data can be obtained free of charge via www.ccdc.cam.ac.uk.

Results and Discussion

Crystal Structure

Complex **1** consists of the trinuclear cyanide-bridged $[\{Mn(L)\}\{Fe(CN)_6\}\{Mn(L)(MeOH)\}]^-$ anion and one isolated $[Mn(L)(MeOH)_2]^+$ cation and two methanol molecules (Fig. 1). The $[Fe(CN)_6]^{3-}$ anion bridge $[Mn(L)]^+$ and $Mn(L)(MeOH)\}]^+$ cations via two C≡N groups in the *cis* positions (Fig. 1). The $[Fe(CN)_6]^{3-}$ fragment exhibits an octahedral coordination, with Fe–C bond lengths are in the range 1.919(12)–1.943(12) Å and Fe–C≡N bond angles in the range 172.7(8)–178.8(10)°. All these parameters are consistent for a low-spin Fe(III), as expected for a cyanide derivative [15–19]. In the $FeMn_2$ fragment, the Mn1 atom exhibits a five-coordinate in a slightly distorted square-pyramidal geometry ($\tau = 0.086$) [30], while the Mn2 atom exhibits a distorted octahedral geometry. The equatorial sites of the Mn1 and Mn2 atoms are occupied by N_2O_2 atoms of the tetradentate Schiff base ligand and one axial position is occupied by a cyanide group of $[Fe(CN)_6]^{3-}$ for Mn1, while two axial positions are occupied by a cyanide group of $[Fe(CN)_6]^{3-}$ and a methanol molecule, respectively. In the isolated $[Mn(L)(MeOH)_2]$ part, Mn3 atom is in a distorted octahedral geometry; the basal plane is occupied by N_2O_2 donor atoms from the tetradentate Schiff base ligand and the two axial positions are occupied by two oxygen atoms from coordinating methanol molecules. Selected bond lengths and angles are listed in Table 2, which are comparable with similar compounds previously reported [15–19]. Each Mn(III) moiety of the complex is nearly coplanar, with a mean deviation from the N_2O_2 plane of 0.002 Å for Mn1, 0.081 Å for Mn2 and 0.002 Å for Mn3, respectively. The dihedral angle between two planes for the $FeMn_2$ fragment is 80.51°. The intramolecular Mn1···Fe1, Mn2···Fe1, and Mn3···Fe1 distances are 4.950 and 5.132, 6.856 Å, respectively. The intramolecular Mn1···Mn2, Mn1···Mn3, and Mn2···Mn3 separations are 7.382, 8.385, and 9.434 Å, respectively. In the crystal packing of complex **1**, the intramolecular and intermolecular O–H···O, O–H···N hydrogen bonds and C–H···π and π···π ring interactions are observed (Table S1, Fig. S1 and Fig. 2). Hydrogen-bonded polymeric networks lie in the *bc* plane and stacks along *a* axis (Fig. S1).

Before proceeding to the spectroscopic, photoluminescence and magnetic studies we note that experimental powder X-ray patterns for **1** are well compatible with those of simulated patterns on the basis of the single crystal structure of **1** (Fig. S2).

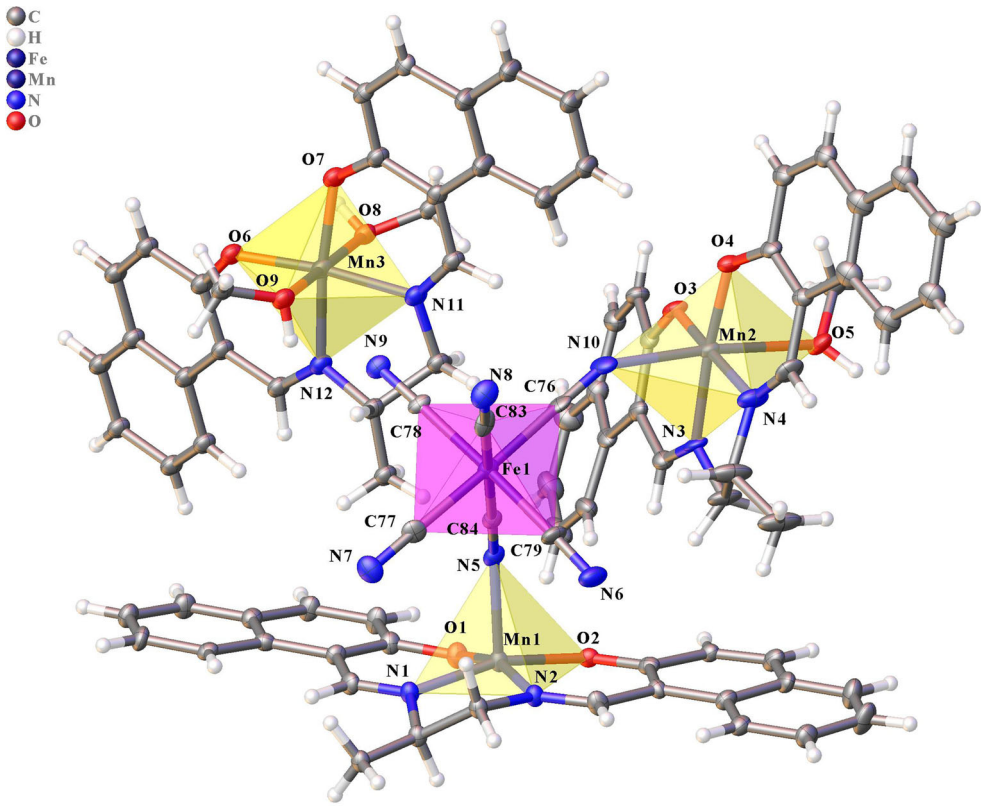

Fig. 1 The molecular structure of **1**. The coordination environment of Fe1, Mn1, Mn2 and Mn3 atoms. Solvent molecules have been omitted for clarity

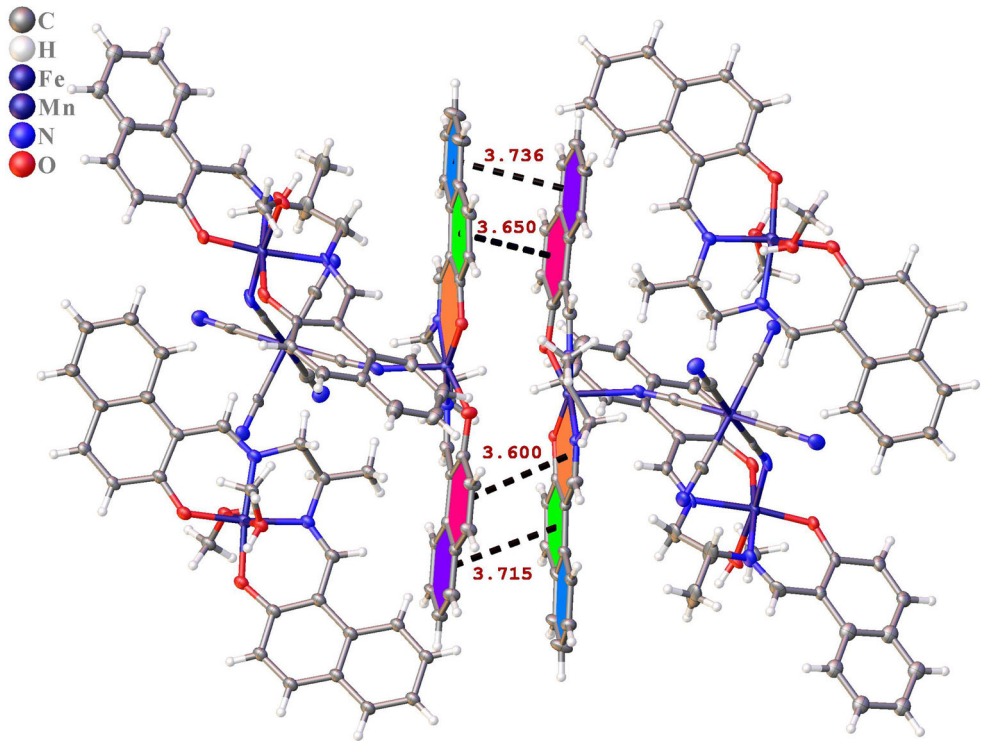

Fig. 2 π···π stacking interactions with the centroid–centroid distances

FT-IR Spectra

In order to find out bond vibration and binding processes for H_2L and **1**, solid state FT-IR spectra which is shown in Fig. S3 have been measured in the range of 4000–600 cm^{-1}. While the spectra were compared by each other, one can conclude that the IR spectra of those structures depict peaks in the nearly similar region. Nevertheless, some significant differences may have been seen in the IR spectra of those structures. While the weak and broad absorption at 3064 cm^{-1} which is attributed to asymmetric and symmetric stretching vibrations of hydroxyl groups ν(O–H) is obtained for the H_2L, this peak is disappeared after complexation which means that some hydroxyl group protons vanished during this process [31, 32]. The absorption at 2108 cm^{-1} is seen for **1**, this stretching vibration band may be assigned as bridging C≡N groups bound to Fe(III) [33]. Two strong and sharp absorption bands in the region 1614–1541 cm^{-1} represent the C=N bridges in the Schiff base ligand [34]. These strong sharp bands are slightly shifted to 1599–1540 cm^{-1} region in **1**. This shifting process can be explained by the coordination of Mn(III) ions with the C = N nitrogen atoms [35].

Solid-state UV–Vis Spectra

To be able to uncover of electronic transitions for the investigated structure, the UV–VIS spectra are measured in the solid state in the range of 200–600 nm as seen from Fig. 3. The high broad absorption band is seen at 388 nm for H_2L. After some chemical process, when the complexation is completed two sharp absorption bands, where are at 310 and 469 nm for **1**, are emerging. When these bands compared with H_2L, one of them shifted to lower and the other one is shifted to higher energy levels. These absorption bands can be attributed $\pi \rightarrow \pi*$ electronic transition associated with the naphthalene rings for the lower one and can be attributed to the d → d transition or Fe(III) → Mn(III) charge transfer (MMCT) transition for the higher one, respectively [36]. The shifting of absorption bands to the lower and higher energy levels in the UV–Vis spectra of **1** signifies the metal ion coordination with H_2L [37].

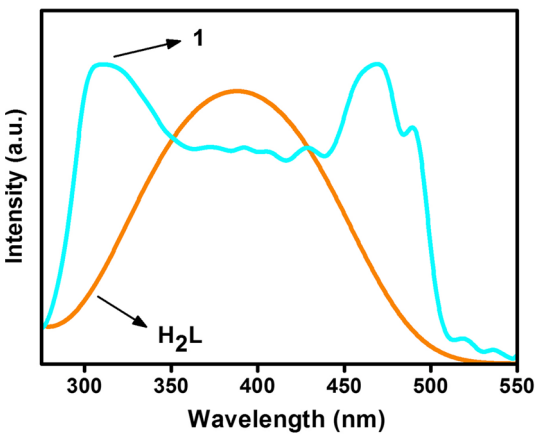

Fig. 3 The solid-state UV–Vis spectrum of H_2L (orange line) and **1** (cyan-blue line) (Color figure online)

Solid-State Photoluminescence Properties

Photoluminescence (PL) spectroscopy is an effective technique commonly used for detection emission process in the crystal structures. In order to determine the emission process of H_2L and **1**, PL spectroscopy was conducted in the visible regions under excitation λ_{ex} = 349 nm at 300 K (Fig. 4). It can be easily seen that the maximum emission intensity of the complex is higher than of the free ligand and both spectra show broad emission bands. The H_2L displays broad weak orange emission band at 620 nm. After complexation, complex **1** shows stronger cyan–blue emission band occurs at 594 nm. It can be concluded that the $\pi \rightarrow \pi*$ inter-ligand electronic transition (ILCT) may be responsible in this emission process and the effect of the bonding metal atom to the ligand may be responsible for the blue shift of the emission peak [38]. The enhancement of luminescence for the complex may be attributed to the chelation of the ligand to the metal atom. The chelation enhances the "rigidity" of the ligand and thus reduces the loss of energy through a radiationless pathway [39].

Magnetic Properties

The temperature dependence of magnetic susceptibility for **1** was measured in the temperature range of 2–300 K an

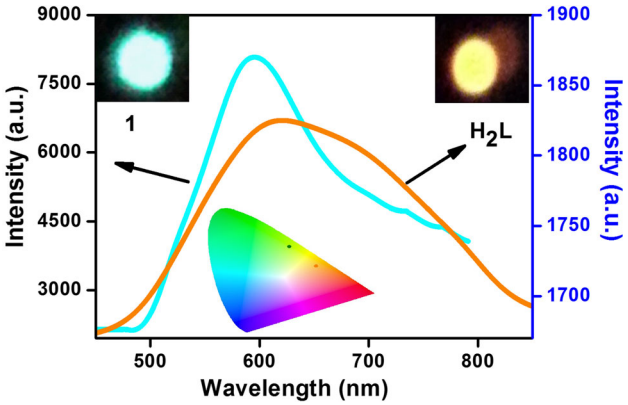

Fig. 4 The solid-state emission spectra of H_2L (orange line) and **1** (cyan line). Upper right and upper-left photos are photoluminescent images of H_2L and **1**, respectively. The middle photo is CIE chromaticity diagram of H_2L and **1** (Color figure online)

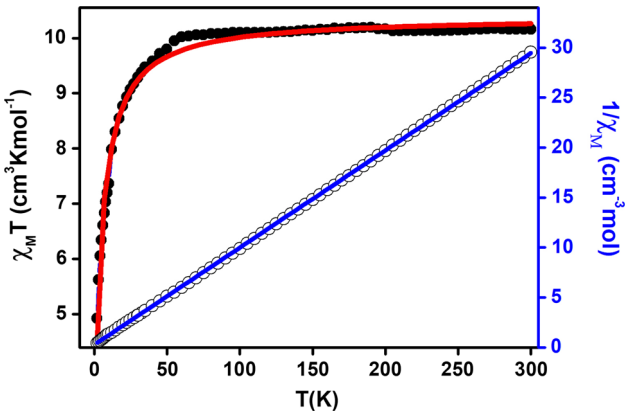

Fig. 5 Temperature dependence of $\chi_M T$ and $1/\chi_M$. The blue line represents the best fit for Curie–Weiss equation (right side), while the solid red line represents the best-fit obtained using Eq. 1 (left side) (Color figure online)

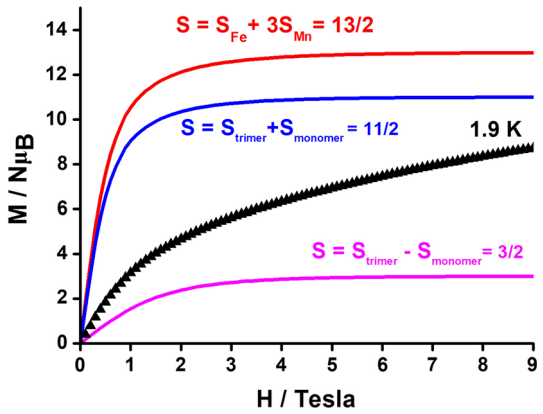

Fig. 6 Field dependence of the magnetization at 1.9 K. The solid lines correspond to the Brillouin curves are given at indicated conditions

applied magnetic field of 1 Tesla, as seen in Fig. 5. The $\chi_M T$ product is almost independent of temperature in the 60–300 K range and then gradually and continuously decreases to 2 K. The $\chi_M T$ value at 300 K is equal to 10.16 cm^3 Kmol^{-1}, which is larger than the spin-only value (9.38 cm^3 Kmol^{-1}) expected for one magnetically isolated low-spin Fe(III) (S = 1/2) and three high-spin Mn(III) ions (S = 4/2) on the basis of g = 2.0, probably because of an orbital contribution to the magnetic moment of the low-spin Fe(III) ion [40]. The plot of $1/\chi_M$ versus T (Fig. 5) obeys the Curie–Weiss law in the range of 2–300 K and give a negative Weiss constant $\theta = -2.60$ K and Curie constant C = 10.27 cm^{3}K/mol. These results indicate the presence of a weak antiferromagnetic interaction between Mn(III) and Fe(III) ions through the C≡N bridge.

The crystal structure of **1** is consist of a Mn_2Fe trinuclear structure linked with C≡N bridge and an isolated Mn(III) mononuclear structure. Because the linear trinuclear structure of Mn(III)–Fe(III)–Mn(III) with the spin system (S_{Mn}, S_{Fe}, S_{Mn}) = (2, 1/2, 2) is symmetric and the magnetic interaction between the terminal Mn(III) ions are neglected, the magnetic properties of the trinuclear structure are interpreted based on the spin Hamiltonian employed was $\hat{H} = -2J(S_{Mn1}S_{Fe} + S_{Mn2}S_{Fe})$. The magnetic susceptibility data can be fitted by combining the trinuclear component (χ_{trimer}) and the monomer contribution ($\chi_{monomer}$) and take into account of the molecular field approximation (zJ′), as given by Eq. 1.

$$\chi_{molecule} = \chi_{trimer} + \chi_{monomer}$$

$$\chi_{trimer} = \frac{Ng^2\mu_B^2}{4kT}\frac{84\left(e^{\frac{-9J}{kT}} + e^{\frac{-7J}{kT}}\right) + 35\left(e^{\frac{-8J}{kT}} + e^{\frac{-2J}{kT}}\right) + 10\left(e^{\frac{-7J}{kT}} + e^{\frac{-3J}{kT}}\right) + \left(e^{\frac{-6J}{kT}} + e^{\frac{-4J}{kT}}\right) + 165}{4\left(e^{\frac{-9J}{kT}} + e^{\frac{-7J}{kT}}\right) + 3\left(e^{\frac{-8J}{kT}} + e^{\frac{-2J}{kT}}\right) + 2\left(e^{\frac{-7J}{kT}} + e^{\frac{-3J}{kT}}\right) + \left(e^{\frac{-6J}{kT}} + e^{\frac{-4J}{kT}}\right) + 5} \quad (1)$$

$$\chi_{monomer} = 2Ng^2b^2/kT$$

$$\chi_m = \chi_{molecule}/\left[1 - (2zJ'/Nb^2g^2)\chi_{molecule}\right]$$

The obtained best fit parameters for the $\chi_M T$ are $g = 2.1$, $J = -1.2$ cm^{-1}, and $zJ' = -0.1$ cm^{-1}, $R^2 = 0.98985$. As a whole, these results indicate a weak antiferromagnetic spin–exchange interaction for complex **1**. The obtained parameters are in good agreement with similar complexes [15–19, 41].

The field dependence of the magnetization at 1.9 K has been measured on a polycrystalline sample of **1** (Fig. 6). The magnetizations observed at 9 Tesla is 8.70 Nμ$_B$. This value is smaller than (11 Nμ$_B$) produced by the Brillouin curve calculated from non-interacting trimer and monomer (S = S_{trimer} + $S_{monomer}$ = 11/2) with g = 2. As seen in Fig. 6, when the field is increased, the magnetization increases gradually and is still rising at the highest measured field (9 Tesla), indicating that saturation has not yet been reached. Such behavior is often observed in $[Mn(SB)]^+$ containing compounds because of the zero-field splitting of the Mn(III) ions, which produces relevant

ZFS of the ground state [21]. However, the theoretical value expected for non-coupled three Mn^{III} ($S_{Mn = 2}$) and one Fe^{III} ($S_{Fe} = 1/2$) ($S = 3S_{Mn} + S_{Fe} = 13/2$) is far away from the observed magnetization value.

Conclusions

In this work, we presented crystal structure, photoluminescence and magnetic characterization of a new tetranuclear cyanide-bridged Mn^{III}–Fe^{III} complex. The DC magnetic measurement of **1** was found to be in good agreement with the literature, and analysis of the data using $\chi_M T$, $1/\chi_m$ and field dependence of the magnetization at 1.9 K indicate an antiferromagnetic coupling for **1**. The solid-state photoluminescence measurements display remarkable cyan-blue emission for **1** and orange emission for its ligand, H_2L, which is attributable to the $n \rightarrow \pi$ or $\pi \rightarrow \pi*$ electronic transition (ILCT). In addition, complex **1** characterized in this study is the second example of cyanide-bridged Mn^{III}–Fe^{III} Schiff base complex which shows luminescence properties. Furthermore, the complex **1** exhibits a strong cyan-blue luminescence emission in the solid state condition at room temperature as seen from the (CIE) chromaticity diagram, and hence the complex may be a promising cyan-blue OLED developing electroluminescent material for flatted or curved panel display applications.

Acknowledgements The authors are grateful to the Research Funds of Muğla Sıtkı Koçman University (BAP–2018/008) for the financial support and Balikesir University, Science and Technology Application and Research Center (BUBTAM) for the use of the Photoluminescence Spectrometer. The authors are also very grateful to Prof. Dr. Andrea Caneschi (Laboratory of Molecular Magnetism, Department of Chemistry, University of Florence) for the use of SQUID magnetometer and helpful suggestions.

References

1. E. Gungor, M. B. Coban, H. Kara, and Y. Acar (2018). *J. Clust. Sci.* **29**, 533.
2. E. Otgonbaatar, M. C. Chung, K. Umakoshi, and C. H. Kwak (2015). *J. Nanosci. Nanotechnol.* **15**, 1389.
3. S. Bibi, S. Mohamad, N. Suhana, A. Manan, J. Ahmad, M. Afzal, S. Mei, B. M. Yamin, and S. N. A. Halim (2017). *J. Mol. Struct.* **1141**, 31.
4. B. Sherino, S. Mohamad, N. Suhana, A. Manan, H. Tareen, B. M. Yamin, and S. N. A. Halim (2017). *Transit. Met. Chem.* **43**, 53.
5. S. Chooset, A. Kantacha, K. Chainok, and S. Wongnawa (2018). *Inorg. Chim. Acta.* **471**, 493.
6. M. B. Coban, E. Gungor, H. Kara, U. Baisch, and Y. Acar (2018). *J. Mol. Struct.* **1154**, 579.
7. J. E. Jee and C. H. Kwak (2013). *Inorg. Chem. Commun.* **33**, 95.
8. S. Kongchoo, K. Chainok, A. Kantacha, and S. Wongnawa (2017). *J. Chem. Sci.* **129**, 431.
9. M. Layek, M. Ghosh, S. Sain, M. Fleck, P. Thomas, S. Jegan, J. Ribas, and D. Bandyopadhyay (2013). *J. Mol. Struct.* **1036**, 422.
10. S. Mandal, A. Kumar, M. Fleck, G. Pilet, J. Ribas, and D. Bandyopadhyay (2010). *Inorg. Chim. Acta.* **363**, 2250.
11. X. Zhou, B. Yu, Y. Guo, X. Tang, H. Zhang, and W. Liu (2010). *Inorg. Chem.* **49**, 4002.
12. Z. Yang, M. She, J. Zhang, X. Chen, Y. Huang, H. Zhu, P. Liu, J. Li, and Z. Shi (2013). *Sensors Actuators B. Chem.* **176**, 482.
13. S. M. Kim, J. Kim, D. Shin, Y. K. Kim, and Y. Ha (2001). *Bull. Korean Chem. Soc.* **22**, 743.
14. L. Yan, R. Li, W. Shen, and Z. Qi (2018). *J. Lumin.* **194**, 151.
15. H. Kara, A. Karaoglu, Y. Yahsi, E. Gungor, A. Caneschi, and L. Sorace (2012). *CrystEngComm* **14**, 7320.
16. E. Gungor, Y. Yahsi, H. Kara, and A. Caneschi (2015). *CrystEngComm* **17**, 3082.
17. M. Zhang, Y. Zhang, C. Yang, and Q. Wang (2016). *Eur. J. Inorg. Chem.* **1**, 3620.
18. D. Pinkowicz, H. I. Southerland, C. Avendan, A. Prosvirin, C. Sanders, W. Wernsdorfer, K. S. Pedersen, J. Dreiser, R. Cle, J. Nehrkorn, G. G. Simeoni, A. Schnegg, K. Holldack, and K. R. Dunbar (2015). *J. Am. Chem. Soc.* **137**, 14406.
19. V. A. Kopotkov, D. V. Korchagin, A. D. Talantsev, R. B. Morgunov, and E. B. Yagubskii (2016). *Inorg. Chem. Commun.* **64**, 27.
20. U. Erkarslan, G. Oylumluoglu, M. B. Coban, E. Öztürk, and H. Kara (2016). *Inorg. Chim. Acta.* **445**, 57.
21. O. Kahn *Molecular Magnetism* (VCH Publishers, New York, 1993).
22. A. Karakuş, A. Elmalı, H. Ünver, H. Kara, and Y. Yahsi (2006). *Z. Naturforsch.* **61b**, 968.
23. E. Gungor and H. Kara (2011). *Spectrochim. Acta - Part A Mol. Biomol. Spectrosc.* **82**, 217.
24. Bruker *APEX2, SAINT and SADABS* (Bruker AXS Inc., Madison, Wisconsin, USA, 2007).
25. G. M. Sheldrick *SADABS* (University of Göttingen, Germany, 2008).
26. G. M. Sheldrick (2008). *Acta Crystallogr. A* **64**, 112.
27. G. M. Sheldrick (2015). *Acta Crystallogr. Sect. C Struct. Chem.* **71**, 3.
28. O. V. Dolomanov, L. J. Bourhis, R. J. Gildea, J. A. K. Howard, and H. Puschmann (2009). *J. Appl. Crystallogr.* **42**, 339.
29. A. L. Spek (2009). *Acta Crystallogr. D. Biol. Crystallogr.* **65**, 148.
30. A. W. Addison, T. N. Rao, J. Reedik, J. van Rijn, and G. C. Verschoor (1984). *J. Chem. Soc. Dalton Trans.* **7**, 1349.
31. C. Kocak, G. Oylumluoglu, A. Donmez, M. B. Coban, U. Erkarslan, M. Aygun, and H. Kara (2017). *Acta Cryst.* **C73**, 414.
32. A. Donmez, M. B. Coban, C. Kocak, G. Oylumluoglu, U. Baisch, and H. Kara (2017). *Mol. Cryst. Liq. Cryst.* **652**, 213.
33. W. Ni, Z. Ni, A. Cui, X. Liang, and H. Kou (2007). *Inorg. Chem.* **46**, 22.
34. Y. Yahsi, E. Gungor, M. B. Coban, and H. Kara (2016). *Mol. Cryst. Liq. Cryst.* **637**, 67.
35. A. Donmez, G. Oylumluoglu, M. B. Coban, C. Kocak, M. Aygun, and H. Kara (2017). *J. Mol. Struct.* **1149**, 569.
36. M. B. Coban (2018). *J. Mol. Struct.* **1162**, 109.
37. M. B. Coban (2017). *J. BAUN Inst. Sci. Technol.* **19**, 7.
38. M. B. Coban, U. Erkarslan, G. Oylumluoglu, M. Aygun, and H. Kara (2016). *Inorg. Chim. Acta.* **447**, 87.
39. X. Feng, Y. Feng, J. J. Chen, S. Ng, L. Wang, and J. Guo (2015). *Dalton Trans.* **44**, 804.
40. H. Miyasaka, N. Matsumoto, N. Re, E. Gallo, and C. Floriani (1997). *Inorg. Chem.* **36**, 670.
41. H. Y. Kwak, D. W. Ryu, J. W. Lee, J. H. Yoon, H. C. Kim, E. K. Koh, J. Krinsky, and C. S. Hong (2010). *Inorg. Chem.* **49**, 4632.